

7-2021

"Super GZK" Particles in a Classic Kramers' Diffusion-over-a-barrier Model. I. The Case of Protons


S. T. Alnussirat

A. F. Barghouty

G. M. Webb

P. L. Biermann

Follow this and additional works at: https://digitalcommons.lsu.edu/physics_astronomy_pubs

 Part of the [Astrophysics and Astronomy Commons](#)



“Super GZK” Particles in a Classic Kramers’ Diffusion-over-a-barrier Model. I. The Case of Protons

S. T. Alnussirat¹, A. F. Barghouty², G. M. Webb³ , and P. L. Biermann^{4,5}

¹ Department of Physics and Astronomy, Louisiana State University, Baton Rouge, LA 70803, USA; alnussirat1@lsu.edu

² NASA Headquarters, Mail Code 7Z58, 300 E St. SW, Washington, DC 20546, USA

³ CSPAR, University of Alabama in Huntsville, Huntsville, AL 35899, USA

⁴ MPI for Radioastronomy, D-53121 Bonn, Germany

⁵ Department of Physics and Astronomy, University of Alabama, Tuscaloosa, AL 35487, USA

Received 2020 December 13; revised 2021 April 30; accepted 2021 May 9; published 2021 June 29

Abstract

In interactions of ultra-high-energy cosmic ray (UHECR) protons with cosmic microwave background photons, we focus in this work on photopion production reactions and the effects of the measured, broad, energy-loss distributions in these reactions on the evolution of the protons’ density functions in energy space. We rely on a Fokker–Planck transport equation in energy space whose transport coefficients are calculated using laboratory measurements. We also derive a Fokker–Planck potential that accounts for both systematic (drift) and stochastic (dispersive) energy losses due to photopion production reactions. Our results show that dispersive energy losses have significant effects on estimating the protons’ horizon distance and their energy spectrum, as well as to elucidate a broadness in the GZK cutoff. We use the derived Fokker–Planck potential to assign a characteristic probability for a proton to clear the potential barrier as a function of energy. This estimate of probability can be used to assist observations in distinguishing between protons and heavy ions as charged particles. Our model is able to account for the so-called super GZK particles as a classic diffusion-over-a-barrier manifestation of the transport of UHECR protons in energy space in quantifying the extent and broadness of the GZK cutoff.

Unified Astronomy Thesaurus concepts: [Ultra-high-energy cosmic radiation \(1733\)](#)

1. Introduction

Ultra-high energy cosmic rays (UHECR; protons and heavier ions with energies in excess of 10^{18} eV) are known to be of extragalactic origin (Hillas 1984; Rachen & Biermann 1993; Rachen et al. 1993; Biermann & Sigl 2001; Berezhko 2008; Biermann et al. 2019; Matthews et al. 2019). However, several fundamental questions remain only partially answered. Questions that pertain to the nature and composition of the primary particles themselves, their astrophysical sources, the acceleration mechanism or mechanisms responsible, and the extent of the influence of propagation effects (for recent reviews, see, e.g., Blümer et al. 2009; Hörandel 2010; Kotera & Olinto 2011; Letessier-Selvon & Stanev 2011; Drury 2012; Biermann et al. 2016). In their journey from their source or sources to observation at Earth, these particles—whether protons or heavier ions—are expected to interact with the cosmic microwave background (CMB) photons, lose enough energy to ultimately suppress their spectra, in what is known as the GZK cutoff (after Greisen 1966 and Zatsepin & Kuz’min 1966). Protons with energies above about 5×10^{19} eV interact with CMB photons and can lose a considerable fraction of their energies. The photopion interaction, e.g., $\gamma_{\text{CMB}} + p \rightarrow \Delta^+ \rightarrow \pi^+ + n$, where n depicts a neutron and Δ nucleon resonance (Hayakawa & Yamamoto 1963; Stecker 1968) is a main channel for this interaction. Heavy ions suffer photodisintegration at somewhat lower energies (Puget et al. 1976; Anchordoqui et al. 1999; Stecker & Salamon 1999). Other sources of energy loss include adiabatic losses due to the intergalactic magnetic field and redshift (Yoshida & Teshima 1993; Protheroe & Johnson 1996; Sigl 2001). For our purposes here, however, these will be ignored. As Berezhinsky & Gazizov (2006, 2007) have shown, for protons with energies above 1×10^{18} eV, and for field strengths of the order of 1 nG with coherent lengths comparable

to the propagation (diffusive) length of the protons in such fields, their motion is rectilinear, even when expansion is taken into account. The smallest proton energy we assume in this analysis is 1.89×10^{19} eV.

While suppression in the spectra of UHECR at energies consistent with the GZK prediction has been observed (Abraham et al. 2008; Abbasi et al. 2009; Apel et al. 2011), attributing unambiguously this suppression to energy losses during propagation or limitations of any acceleration mechanism at the source remains largely model dependent (Mücke et al. 1999; Boratav & Letessier-Selvon 2001; Haungs et al. 2003; Grigor’eva 2007; Drury 2012; Berezhinsky 2013; Blaksley et al. 2013; Kampert 2013; Harari 2014).

Recent analysis of the Telescope Array (Abbasi et al. 2014) and Pierre Auger Observatory (Aab et al. 2018) data show an indication of anisotropy in the source distribution for particle energy around 8 EeV. Additionally, a simulation study by Wittkowski & Kampert (2018) has shown a suggestion of pronounced dipolar anisotropy in the arrival direction of UHECR for energies >15 EeV. This sky anisotropy indicates that UHECR sources are within the GZK horizon (100 Mpc distance) with some possible sources as close as 5 Mpc.

This work explores the effects of systematics in the energy-loss rate on the UHECR protons propagation from a purely kinetics viewpoint, i.e., a Fokker–Planck equation in distance-energy space with the assumption of applicability of the diffusion formalism (Aloisio et al. 2009). We explicitly take dispersion in the energy loss of the protons in the reaction’s three main channels: $p + \gamma_{\text{CMB}} \rightarrow \pi^+ + n$, $p + \gamma_{\text{CMB}} \rightarrow \pi^0 + p$, and $n + \gamma_{\text{CMB}} \rightarrow \pi^- + p$ into account, where they collectively amount to more than 88% of the total reaction cross-section $\sigma_{\text{total}}(E)$ (Armstrong et al. 1972; Genzel et al. 1973), with E being the UHECR proton total energy. For that we rely fully on

the measured interaction double-differential cross-section, $d\sigma/d\Omega$. These measurements are made in the proton's rest frame with photon beams of 0.3–1 GeV in energy (Armstrong et al. 1972). The energy-loss rate and its dispersion are calculated from the measured double-differential cross-sections and the assumed, standard CMB energy distribution to arrive at our Fokker–Planck transport coefficients, $\langle\Delta E\rangle/\Delta s$ and $\langle(\Delta E)^2\rangle/\Delta s$ in energy space, where ΔE is the energy loss and Δs is pathlength increment along the interaction pathlength, s , to the source.

The derived energy-transport Fokker–Planck equation is then transformed into a form suitable for the derivation of the Fokker–Planck potential (Kramers 1940; Gardiner 1983; Risken 1989; Hanggi et al. 1990) for UHECR. Our analysis relies on this potential in two main ways. (1) Dispersions in energy loss enter the potential explicitly, hence, so do their effects on any calculated transport quantity. (2) Probability and kinetic measures associated with the motion of UHECR protons in energy space follow immediately from this potential. While simulations and semianalytic studies of the propagation of UHECR protons do take their energy losses into account (Yoshida & Teshima 1993; Protheroe & Johnson 1996; Mücke et al. 2000; Sigl 2001; Batista et al. 2016), the potential approach can offer insights (along with their likelihoods) to help differentiate among competing models in the analysis of UHECR data and phenomenology.

2. Description of the Model

2.1. Derivation of the Fokker–Planck Transport Coefficients in Energy Space

The Fokker–Planck drift (or systematic energy-loss rate, $\mathcal{K}_1(E)$) and diffusion (energy-loss dispersion rate, $\mathcal{K}_2(E)$) are derived from the measured (Genzel et al. 1973) double-differential cross-sections $d\sigma_i/d\Omega$, where i refers to one of three main reaction channels: $p + \gamma_{\text{CMB}} \rightarrow \pi^+ + n$, $p + \gamma_{\text{CMB}} \rightarrow \pi^0 + p$, and $n + \gamma_{\text{CMB}} \rightarrow \pi^- + p$, and where such measurements are made in the rest frame of the proton. In the laboratory frame, the energy-loss rate is calculated as

$$\frac{\langle\Delta E\rangle}{\Delta s}(E) = \int \int \frac{d\sigma}{dE'}(E', E, E_\gamma) \rho(E_\gamma)(E - E') dE' dE_\gamma, \quad (1)$$

where $\Delta E = E - E'$, $d\sigma/dE'$ is the energy-loss cross-section for each reaction channel, which is a function of $E'(<E)$, the energy of the proton after its collision with the CMB photon, the proton's initial energy E , and the CMB photon's energy E_γ . $\rho(E_\gamma)$ is the CMB photon energy density. (Note that since c , speed of light, is also essentially the relative velocity between the proton and CMB photon in the laboratory frame, the relative velocity term in Equation (1) above cancels out when we write $\Delta s = c \Delta t$, with t being the proper time).

Following Hill & Schramm (1985), we use temperature-scaled, nondimensionalized energy units, where we define, $\epsilon = E k_B T/m_o^2$, $\epsilon' = E' k_B T/m_o^2$, and $\epsilon_\gamma = E_\gamma/k_B T$, $\Delta\epsilon = \epsilon - \epsilon'$, with k_B being Boltzmann's constant, m_o being the nucleon's rest mass, and T being the CMB photons' blackbody temperature. Kinematically we can relate $d\sigma/dE'$ in Equation (1) above to the measured double-differential cross-section $d\sigma^{(\text{cm})}/d\Omega$ in the center-of-mass frame, in which frame measurements are also expressed. In these scaled energy units, the

measured, parameterized double-differential cross is written as (Genzel et al. 1973; Hill & Schramm 1985):

$$\frac{d\sigma}{d\epsilon'} = \sum_{n=0}^N a_n \left(\frac{2}{\epsilon'^+ - \epsilon'^-} \right) \left[\frac{2\epsilon - (\epsilon'^+ + \epsilon'^-)}{\epsilon'^+ - \epsilon'^-} \right]^n, \quad (2)$$

where a_n are the expansion coefficients in the cosine of the pion's angle in the center-of-mass system, and ϵ'^+ (ϵ'^-) are upper (lower) kinematic limits for the proton (or neutron) in the same frame. These limits were derived by Hill & Schramm (1985) as:

$$\epsilon'^{\pm} = \epsilon \times \left\{ \frac{2\epsilon\epsilon_\gamma + 1 - m_\pi^2/(2m_o^2)}{4\epsilon\epsilon_\gamma + 1} \pm \frac{[(2\epsilon\epsilon_\gamma - m_\pi^2/(2m_o^2))^2 - m_\pi^2/m_o^2]^{1/2}}{4\epsilon\epsilon_\gamma + 1} \right\}, \quad (3)$$

where m_π is the pion's rest mass. In the same scaled energy units, the CMB photons' energy density we use (Hill & Schramm 1985) is written as

$$\rho(\epsilon_\gamma) = \frac{n_\gamma}{2\pi^2} \epsilon_\gamma^2 \int_1^\infty \frac{\zeta}{\exp(\zeta\epsilon_\gamma/2) - 1} d\zeta, \quad (4)$$

with n_γ being the CMB photon number density.

In such units, the energy-loss rate is now written as

$$\begin{aligned} & \frac{\langle\Delta\epsilon\rangle}{\Delta s}(\epsilon) \\ &= \text{const} \int_{\epsilon_\gamma, \min}^{\epsilon_\gamma, \max} \int_{\epsilon'^-}^{\epsilon'^+} \frac{d\sigma}{d\epsilon'}(\epsilon', \epsilon, \epsilon_\gamma) \rho(\epsilon_\gamma) \Delta\epsilon d\epsilon' d\epsilon_\gamma, \end{aligned} \quad (5)$$

where the constant is on the order of 10^{-4} when Δs is expressed in Mpc and all energies in the temperature-scaled units. ϵ_γ, \min is a lower limit on the energy of the photon, which we set arbitrarily to $0.19/\epsilon$ so as to keep the kinematic limits of Equation (3) real. The upper limit is set to $0.64/\epsilon$ for the same reason.

Similar to Equation (5), the energy-loss dispersion rate in scaled energy units is written,

$$\begin{aligned} \mathcal{K}_2(\epsilon) &= \frac{\langle(\Delta\epsilon)^2\rangle}{\Delta s}(\epsilon) = \text{const} \int_{\epsilon_\gamma, \min}^{\epsilon_\gamma, \max} \int_{\epsilon'^-}^{\epsilon'^+} \frac{d\sigma}{d\epsilon'} \\ &\times (\epsilon', \epsilon, \epsilon_\gamma) \rho(\epsilon_\gamma) (\Delta\epsilon)^2 d\epsilon' d\epsilon_\gamma. \end{aligned} \quad (6)$$

In scaled energy units, the Fokker–Planck transport equation in energy space can now be expressed as,

$$\frac{\partial f}{\partial s} = -\frac{\partial}{\partial\epsilon}[\mathcal{K}_1(\epsilon)f(\epsilon, s)] + \frac{\partial^2}{\partial\epsilon^2}[\mathcal{K}_2(\epsilon)f(\epsilon, s)], \quad (7)$$

where ds is the differential pathlength and $\mathcal{K}_1(\epsilon) = -\frac{\langle\Delta\epsilon\rangle}{\Delta s}(\epsilon)$.

Shown in Figure 1 are the differential energy-loss cross-section $d\sigma/d\epsilon'$ as a function of energy at three incident proton energies: $\epsilon = 0.5$ (1890 EeV); $\epsilon = 0.2$ (757 EeV); and $\epsilon = 0.08$ (302 EeV). For each incident energy, shown in red is the sum of the three processes' differential energy-loss cross-section, where green depicts $d\sigma/d\epsilon'$ for the reaction $\gamma_{\text{CMB}} + p \rightarrow \pi^+ + n$, blue for $\gamma_{\text{CMB}} + p \rightarrow \pi^0 + p$, and brown for $\gamma_{\text{CMB}} + n \rightarrow \pi^- + p$. Each differential cross-section was estimated using the parameterization in Equation (2) where the expansion

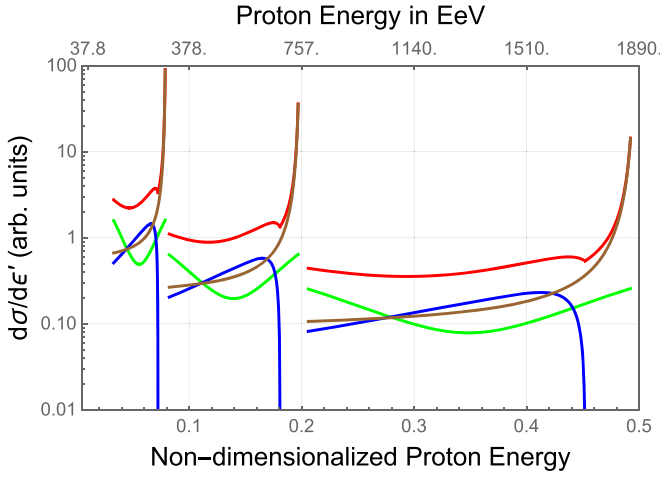


Figure 1. Data-based estimated differential energy-loss cross-section $d\sigma/d\epsilon'$ as a function of energy at the three incident proton energies: $\epsilon = 0.5$ (1890 EeV); $\epsilon = 0.2$ (757 EeV); and $\epsilon = 0.08$ (302 EeV). For each incident energy, shown in red is the sum of the three processes' differential energy-loss cross-section where green depicts $d\sigma/d\epsilon'$ for the reaction $\gamma_{\text{CMB}} + p \rightarrow \pi^+ + n$, blue for $\gamma_{\text{CMB}} + p \rightarrow \pi^0 + p$, and brown for $\gamma_{\text{CMB}} + n \rightarrow \pi^- + p$. (See the text for details.)

coefficients a_n are taken from measurements (Genzel et al. 1973) up to and including the third, $n = 2$, term.

Figure 2 shows the calculated (discrete points) energy-loss rate, according to Equation (5). The dashed curve is a best fit to these points;

$$|\mathcal{K}_1(\epsilon)| \approx c_1 \arctan(c_2 \epsilon^{c_3}), \quad (8)$$

with $c_1 = 0.0123 \text{ Mpc}^{-1}$, $c_2 = 15.65$, and $c_3 = 1.325$. Similarly, Figure 3 shows the calculated (discrete points) Fokker-Planck diffusion coefficient, $\mathcal{K}_2(\epsilon)$, according to Equation (6). The dashed curve is a best fit to these points:

$$\mathcal{K}_2(\epsilon) \approx \frac{d_1 \epsilon^2}{d_2 + d_3 \epsilon^2}, \quad (9)$$

with $d_1 = 95.344 \text{ Mpc}^{-1}$, $d_2 = 5272.7$, and $d_3 = 24714$. It can be seen from Figure 3 that the diffusive energy losses become important at high energies. However, the propagation effect is a function of proton energy and propagation distance.

Since both the systematic and stochastic energy losses are purely collisional in our model, we can estimate a characteristic dispersive energy-loss distance by noting that the characteristic energy-loss scale is $\sim \sqrt{2} \mathcal{K}_2(\epsilon)/\mathcal{K}_1(\epsilon)$ (Payne 1969; Tsendin 2006). Dividing this energy-loss scale by $\mathcal{K}_1(\epsilon)/\sqrt{2}$ should give a corresponding characteristic dispersive energy-loss distance. Using these coefficients we can estimate a characteristic dispersive distance, $\ell(\epsilon)$, using:

$$\ell(\epsilon) = \frac{2\mathcal{K}_2(\epsilon)}{\mathcal{K}_1^2(\epsilon)}. \quad (10)$$

The calculated $\ell(\epsilon)$ is shown in Figure 4, which can be considered as a distance scale to measure the importance of diffusive energy losses, as a function of proton energy. If a proton with energy ϵ is propagating from a source located at a distance s Mpc, the characteristic dispersive attenuation distance is $\ell(\epsilon)$. As an example, for a proton with energy $\epsilon = 0.01$ this characteristic distance is ≈ 19.5 Mpc, while it is ≈ 5.5 Mpc for a proton with energy $\epsilon = 0.1$. If these two protons were to propagate 10 Mpc distance, then the effect of

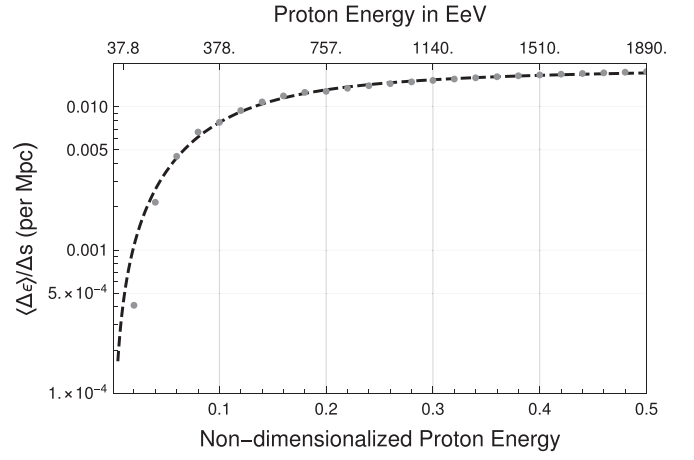


Figure 2. The energy-loss rate calculated using Equation (5) (discrete points). The dashed curve is a best fit to these points.

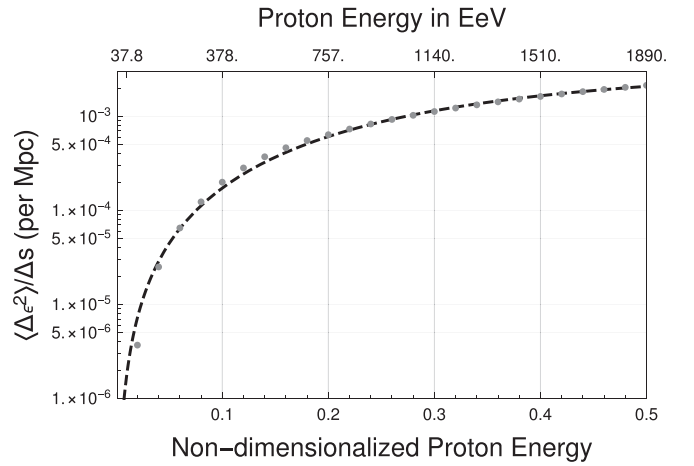


Figure 3. The Fokker-Planck diffusion coefficient calculated using Equation (6) (discrete points). The dashed curve is a best fit to these points.

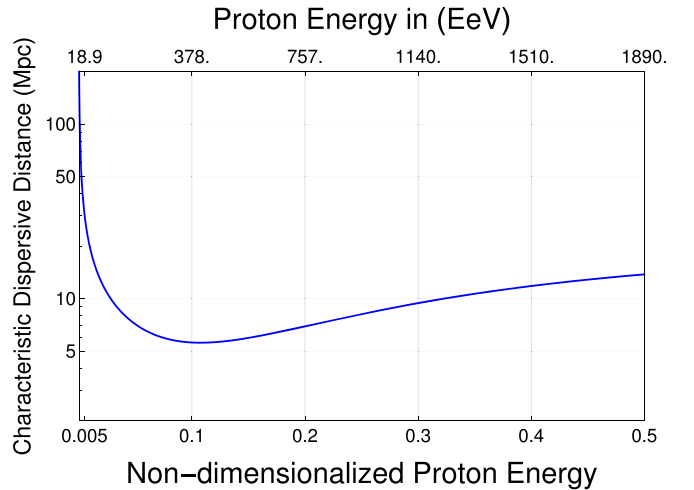


Figure 4. The characteristic dispersive energy-loss distance as a function of energy.

dispersion in their respective energy losses is more important for the proton that has $l = 5.5$ Mpc. Figure 4 also suggests that over a rather wide energy range, $\epsilon \in [0.05, 0.5]$, ℓ changes only by a factor of 2. Given the definition of ℓ this suggests that

dispersion in energy loss remains equally important as the systematic energy loss over this large dynamic energy range. We expound on this feature and implications to the GZK cutoff in Section 2.3. As a result, when studying the transport of UHECR protons, their energy loss and propagation distance cannot be fully separated. In other words, the importance of dispersion in energy losses is determined by the primary proton's energy as well as propagation distance.

2.2. Derivation of the Fokker–Planck Potential

To derive the Fokker–Planck potential, Equation (7) needs to be re-expressed with a constant diffusion coefficient (Risken 1989) using the transformation in the independent variables, $\epsilon \rightarrow \xi$ (see the Appendix):

$$\left(\frac{d\xi}{d\epsilon}\right)^2 \times \mathcal{K}_2(\epsilon) = \mathcal{K}'_2 = \text{constant}, \quad (11)$$

which gives, for $d\mathcal{K}'_2/d\epsilon = 0$ over a finite domain for $\epsilon \in [0.005, 0.5]$,

$$\xi(\epsilon) = \int_{0.005}^{\epsilon} \left(\frac{\mathcal{K}'_2}{\mathcal{K}_2(\zeta)}\right)^{1/2} d\zeta. \quad (12)$$

The transformed drift term is given by

$$\mathcal{K}'_1[\xi(\epsilon)] = \left(\frac{\mathcal{K}'_2}{\mathcal{K}_2(\epsilon)}\right)^{1/2} \left(\mathcal{K}_1(\epsilon) - \frac{1}{2} \frac{d\mathcal{K}_2(\epsilon)}{d\epsilon}\right). \quad (13)$$

In terms of the new independent variable, ξ , and the dependent variable, $\tilde{f}(\xi, s)$, Equation (7) is written (note though that the time-like variable, s , remains the same),

$$\frac{\partial \tilde{f}(\xi, s)}{\partial s} = -\frac{\partial}{\partial \xi} [\mathcal{K}'_1(\xi) \tilde{f}(\xi, s)] + \mathcal{K}'_2 \frac{\partial^2 \tilde{f}(\xi, s)}{\partial \xi^2}. \quad (14)$$

In formal analogy with the Hamiltonian operator (Englefield 1988; Risken 1989),

$$\mathcal{H} = -V(\xi) + \mathcal{K}'_2 \frac{\partial^2}{\partial \xi^2}, \quad (15)$$

where \mathcal{K}'_2 is an arbitrary constant and $V(\xi)$ is a single-particle Schrodinger potential, we can define a Fokker–Planck “potential” as

$$\phi(\xi) = -\int^{\xi} \mathcal{K}'_1[\xi'] d\xi', \quad (16)$$

which is related to the Schrodinger potential by $V(\xi) = 1/(4\mathcal{K}'_2)(d\phi/d\xi)^2 - (1/2)d^2\phi/d\xi^2$. A connection between the Fokker–Planck and Schrodinger equations can help guide solutions, because large number solutions exist for quadratic and cubic potential, as well demonstrated by Englefield (1988). In terms of the Fokker–Planck potential, Equation (14) becomes:

$$\frac{\partial \tilde{f}(\xi, s)}{\partial s} = \frac{\partial}{\partial \xi} \left[\frac{\partial \phi(\xi)}{\partial \xi} \tilde{f}(\xi, s) \right] + \mathcal{K}'_2 \frac{\partial^2 \tilde{f}(\xi, s)}{\partial \xi^2}. \quad (17)$$

Figure 5 shows the derived Fokker–Planck potential using Equations (13) and (16) and setting $\mathcal{K}'_2 = \frac{1}{2}$. We numerically solved for the energy points $\epsilon \in [0.005, 0.5]$, which correspond to

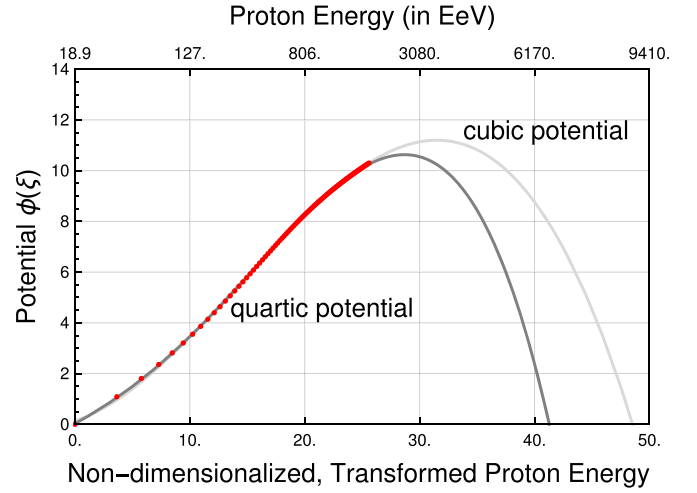


Figure 5. The derived Fokker–Planck potential (discrete points). The solid dark curve is a fourth-order polynomial fit to the discrete points and the solid lighter curve is a third-order polynomial fit to the same points. ξ is a non-dimensionalized and transformed proton energy (see the text).

$\xi \in [0.0, 25.6]$ and $E \in [1.89 \times 10^{19}, 1.89 \times 10^{21}]$ eV, where data are available, that satisfy Equations (13) and (16) simultaneously. The darker solid curve is a fourth-order polynomial fit to the calculated discrete points. The light solid curve is a third-order polynomial fit to the same points. The fourth-order fit is given by $\phi^{(4)}(\xi) = -17.309 \times 10^{-6} \xi^4 + 0.000399 \xi^3 + 0.00693 \xi^2 + 0.251 \xi + 0.0265$. The third-order fit is given by $\phi^{(3)}(\xi) = -5.644 \times 10^{-4} \xi^3 + 0.0244 \xi^2 + 0.142 \xi + 0.142$. The quartic potential has a zero at $\xi = \xi_{\text{max}} = 41.281$ (6.58×10^{21} eV), and a maximum at $\xi = \xi_m = 28.67$ (2.70×10^{21} eV). The value of the quartic potential at maximum is 10.63, in units of ξ^2 per Mpc, which are the same units \mathcal{K}'_2 is expressed as unity in. Similarly, the cubic potential has a zero at $\xi = \xi_{\text{max}} = 48.54$ (8.93×10^{21} eV), and a maximum at $\xi = \xi_m = 31.49$ (3.51×10^{21} eV). The value of the cubic potential at maximum is 11.19 in units of ξ^2 per Mpc. The two fits are statistically different, the error sum of squares (SSE) for the quartic fit is 0.0385 while it is 0.129 for the cubic fit. Thus, the quartic fit is more significant and is the one we use to carry out the numerical solution of Equation (14) in Section 3. However, both fits are identical in the energy range of interest and we use both of them to estimate the horizon distance and probability to clear the potential barrier.

2.3. The Fokker–Planck Potential and the UHECR Proton's Horizon Distance

Next we estimate the mean distance, as a function of the proton energy it takes the UHECR proton to overcome this potential barrier, i.e., to go from the energy at which the potential is maximum, which is at $\xi = \xi_m$, to the equilibrium point of the potential at $\xi = 0$. This distance, which we call $\mathcal{S}(\xi)$, is calculated using two different approaches. In the first approach we follow the same formalism (Gardiner 1983) typically used to calculate the mean first passage time,

$$\mathcal{S}(\xi) = \frac{1}{\mathcal{K}'_2} \int_{\xi}^{\xi'} \int_{\xi_m}^{\xi'} \exp(+\phi(\xi'')/\mathcal{K}'_2) \times \exp(-\phi(\xi''')/\mathcal{K}'_2) d\xi'' d\xi'''. \quad (18)$$

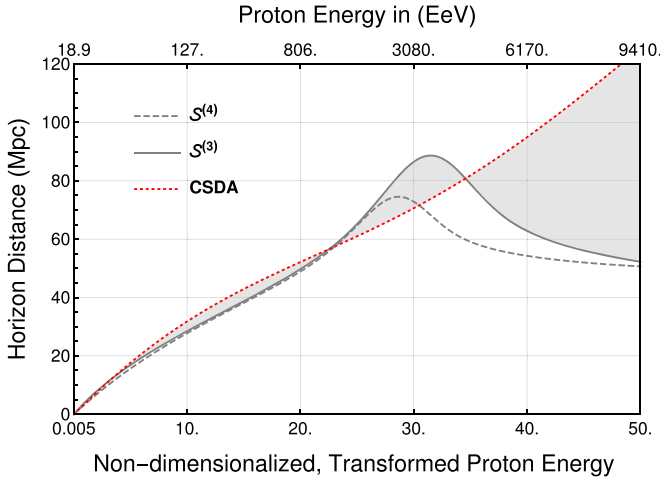


Figure 6. The calculated mean horizon distance in Mpc for a proton with energy ξ to clear the Fokker–Planck potential $\phi(\xi)$. The solid dark curve corresponds to the third-order polynomial fit to the potential, the dashed gray curve to the fourth-order polynomial fit, and the dashed red curve to calculations based on the continuous-slowing-down approximation (CSDA).

Note that the expression for $\mathcal{S}(\xi)$ above is a solution to the second-order ODE (Hanggi et al. 1990):

$$\mathcal{K}_2' \frac{d^2 \mathcal{S}}{d\xi^2} - \frac{d\phi(\xi)}{d\xi} \frac{d\mathcal{S}(\xi)}{d\xi} = -1, \quad (19)$$

where $\xi \in [0, \xi_m]$, and where we assume that $\mathcal{S} \rightarrow 0$ at $\xi = 0$, i.e., an absorbing boundary, and $d\mathcal{S}/d\xi \rightarrow 0$ at $\xi = \xi_m$, a reflecting boundary.

The second approach is based on the continuous-slowing-down approximation (CSDA), where $\mathcal{S}(\xi)$ is calculated using:

$$\mathcal{S}^{\text{CSDA}}(\xi) = \int_{\xi}^0 \frac{d\xi'}{\mathcal{K}_1(\xi')}. \quad (20)$$

Calculating the horizon distance using Equation (18) involves both the systematic and stochastic energy losses in a compact form (the potential form), while the CSDA calculations involve only the systematic energy losses. Two horizon distances result from Equation (18); $\mathcal{S}^{(3)}(\xi)$ results from using the third-order potential fit, $\phi^{(3)}$, and similarly, $\mathcal{S}^{(4)}(\xi)$ is the horizon distance that results from the fourth-order potential fit, $\phi^{(4)}$.

Figure 6 shows the calculated mean horizon distance, $\mathcal{S}(\xi)$, as a function of proton energy. Several defining characteristics can be seen. First, the two potential fits seem to give very similar distance-versus-energy curves, as their behavior is essentially the same except for energies at and higher than about $\xi \approx 27$ (2.2×10^{21} eV). Distance inferred from the cubic potential, $\mathcal{S}^{(3)}$, reaches a maximum of around 88 Mpc at an energy of about $\xi = 32$ (3.67×10^{21} eV), while $\mathcal{S}^{(4)}$ reaches its maximum of about 75 Mpc at $\xi = 28$ (2.51×10^{21} eV). The maximum horizon distance corresponds to an energy that maximizes the potential. Noting that the ratio of the two potentials' heights, $\phi_{\text{max}}^{(3)}/\phi_{\text{max}}^{(4)}$, is only about 1.05, which translates to $\sqrt{1.05}$ along ξ , while the ratio of their widths at equilibrium, $\xi_m^{(3)}/\xi_m^{(4)}$ is about 1.2, for this high energy regime the distance inferred from the potential appears more sensitive to the width of the potential than its height.

Two energy regimes can be seen from Figure 6. For energies up to about $\xi \approx 25$ (1.75×10^{21} eV), and for both potentials $\mathcal{S}(\xi)$

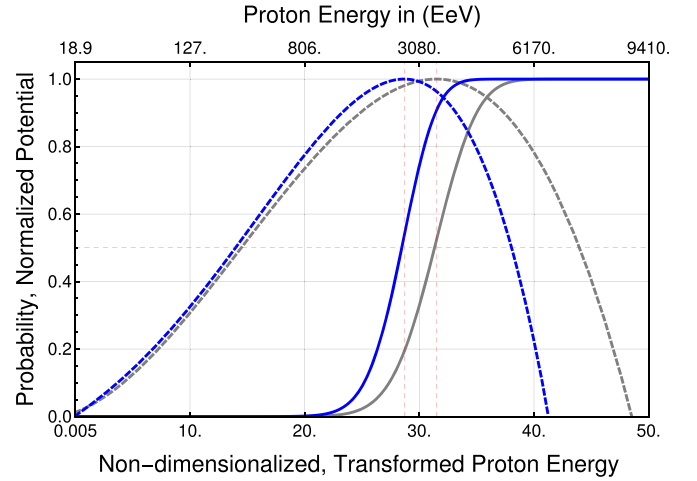


Figure 7. The calculated probability for a proton with energy ξ to clear the Fokker–Planck potential $\phi(\xi)$. Dashed gray and blue curves show the third- and fourth-order polynomial fits of the potential (normalized to unity), respectively. Solid gray and blue curves show the probability for a proton to clear the Fokker–Planck potential corresponding to the third- and fourth-order polynomial fits, respectively. The vertical dashed red lines correspond to the fitted potentials' maximum and the horizontal dashed line indicates a probability of 0.5.

appears to rise exponentially with ξ . For energies between $\xi \approx 25$ and $\xi \approx 35$ (1.75×10^{21} eV– 4.58×10^{21} eV), the rise reaches a maximum then a drop in the horizon distance is seen.

Additionally, we note that the inferred distance for both potentials increases by only a factor of 3 in about 2 orders of magnitude in proton energy; from 20 Mpc at $\xi = 5$ (4.89×10^{19} eV) to 60 Mpc at $\xi = 25$ (1.75×10^{21} eV). This clearly suggests that the GZK cutoff is quite broad. We quantify the degree of this broadness in Section 2.4.

Figure 6 also shows the calculated horizon distance based on the CSDA approximation, which is purely determined by the systematic energy losses. A difference between the calculated horizon distances with and without the diffusive energy-loss effects are seen at high energies. As can be seen from Figures 3 and 4, stochastic energy losses are important at high energies; so at high enough energies the diffusive effect is dominant and has a clear impact on the horizon distance calculations. These are indicators of the importance of dispersion in energy losses in UHECR propagation. Likewise, we expect to see an energy-loss dispersion effect on the protons' energy spectrum, which we address in Section 3.

2.4. The Fokker–Planck Potential and the GZK Cutoff

In addition to the horizon distance, using the derived Fokker–Planck potential we can explicitly calculate the likelihood of a proton at a certain energy ($\xi > 0$) reaching the lower limit of the ξ -domain, which we set to zero (see Section 2.2). This probability measure is calculated using (Gardiner 1983):

$$\mathcal{M}(\xi) = \frac{\int_0^\xi \exp(+\phi(\xi')/\mathcal{K}_2') d\xi'}{\int_0^{\xi_{\text{max}}} \exp(+\phi(\xi'')/\mathcal{K}_2'') d\xi''}. \quad (21)$$

Figure 7 shows the calculated probability for a proton with energy ξ to clear the Fokker–Planck potential $\phi(\xi)$. This figure shows that if a particle with energy less than $\xi \approx 20$ (8.05×10^{20} eV) cleared the potential barrier, then the probability of this particle being a proton is almost zero, and hence, it is more likely

to be a heavy ion if a charged particle is observed at this energy. Conversely, at much higher energies, $\xi > 35$ (4.58×10^{21} eV), there is almost a 100% chance that these particles are protons. This estimated probability agrees with the fact that heavy ions would have experienced photodisintegration below this energy. On the other hand, if a charged particle with energy $\xi \approx 30$ (3.08×10^{21} eV) is observed, then there is around 50% probability for this particle to be a proton and 50% probability for it to be a heavy ion. Previous analysis of the Pierre Auger Observatory measured composition indicates heavier elements at energies beyond 2×10^{18} eV. Additionally, Aab et al. (2014, 2016) concluded that this fraction of the spectrum being proton is zero above 10^{19} eV with an indication of higher fractions at higher energies. These findings are qualitatively consistent with Figure 7.

This estimated probability is for protons at steady-state. In order to compare our model results with other experiments, similar calculations as a function of distance are needed. Additionally, similar calculations are needed for each heavy ion. This will enable a more precise interpretation of the observations and identify particles based on their energies. Unfortunately, these calculations are not available at present due to the dearth of knowledge of measured photodisintegration differential cross-section of many heavy ions of interest. However, Figure 7 can still be used to distinguish between protons and heavy ions as observed charged particles.

3. Solution of the Fokker–Planck Equation

The transformed Fokker–Planck transport equation in energy space (Equations (7) and (16)) is used to study the spatial evolution of the proton’s energy spectrum. In what follows we discuss three different cases: the steady-state, nondispersive, and spatially dependent solutions.

At steady-state ($\frac{\partial \tilde{f}}{\partial s} = 0$), Equation (17) reads:

$$\frac{d}{d\xi} \left[\frac{\partial \phi(\xi)}{\partial \xi} \tilde{f}_s(\xi) \right] + \mathcal{K}'_2 \frac{d^2}{d\xi^2} [\tilde{f}_s(\xi)] = 0, \quad (22)$$

where $\tilde{f}_s(\xi)$ is the steady-state proton energy spectrum. Equation (22) can be written as a continuity equation

$$\frac{d}{d\xi} [j(\xi)] = 0, \quad (23)$$

with the flux $j(\xi)$ defined as:

$$j(\xi) = \frac{\partial \phi(\xi)}{\partial \xi} \tilde{f}_s(\xi) + \mathcal{K}'_2 \frac{d}{d\xi} [\tilde{f}_s(\xi)]. \quad (24)$$

From Equation (23) the solution is $j(\xi) = \text{constant}$. For zero flux boundary conditions, the steady-state solution (potential solution) is given by:

$$\tilde{f}_s(\xi) = N \exp\left(\frac{-\phi(\xi)}{\mathcal{K}'_2}\right), \quad (25)$$

where N is chosen to satisfy:

$$\int_{\xi_{\min}}^{\xi_{\max}} \tilde{f}_s(\xi) d\xi = 1. \quad (26)$$

In addition to the steady-state solution, we use Equation (17) to study the spatial evolution of the proton energy spectrum

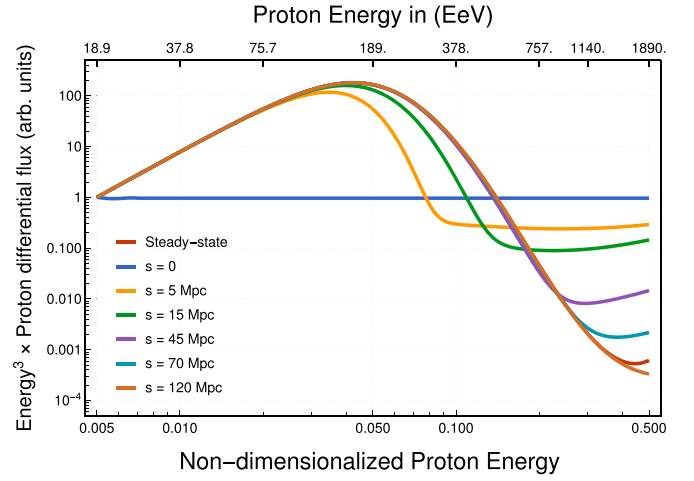


Figure 8. The steady-state potential solution and the spatial evolution of protons’ spectrum for different source distances.

under the effect of the systematic and dispersive energy losses (in the potential form). To obtain a solution of Equation (17) we use the numerical method of lines (Schiesser 1992) with an initial condition in the transformed variable ξ that corresponds to $f(\epsilon, s = 0) \propto \epsilon^{-3}$. The boundary conditions are chosen to be reflecting at $\xi = \xi_{\min}$ and zero flux at $\xi = \xi_{\max}$.

Finally, we use Equation (7) to study the protons’ energy spectrum under the assumption of $\mathcal{K}_2(\epsilon) = 0$. In this case Equation (7) becomes:

$$\frac{\partial f}{\partial s} = \frac{\partial}{\partial \epsilon} [\mathcal{K}_1(\epsilon) f(\epsilon, s)], \quad (27)$$

with an initial condition $f(\epsilon, s = 0) = N_0 \epsilon^{-\eta}$, where $\eta = 3$. The solution of Equation (27) using the method of characteristics is given by:

$$f(\epsilon, s) = N_0 \left(\epsilon + \frac{\partial \mathcal{K}_1(\epsilon)}{\partial \epsilon} \right)^{-\eta} \exp[s \mathcal{K}_1(\epsilon)]. \quad (28)$$

Figure 8 compares the steady-state (Equation (25)) and the numerical solutions to Equation (17) at $s = 0, 5, 15, 45, 70,$ and 120 Mpc. As can be seen from the figure, the numerical solution matches the steady-state solution at large propagation distances ($s > 70$ Mpc).

Figure 9 compares the steady-state, numerical, and non-dispersive solutions for the propagation distances $s = 10$ and 120 Mpc. At $s = 120$ Mpc, the numerical solution is seen to approach the steady-state one. A notable difference between the steady-state (Equation (25)) and nondispersive (Equation (28)) cases is also seen. This difference is due to energy-loss dispersion effects. Figures 8 and 9 suggest that two factors contribute to the protons’ energy spectrum: nondispersive and dispersive effects. Fedorov et al. (2016) suggest that dispersive and nondispersive effects, for spatial evolution, appear to affect the proton’s spectrum. We will address the same for energy in a future work.

As gleaned from Figure 8, each propagation distance shows a characteristically different proton energy spectrum. Each energy spectrum has a maximum at a different energy. Figure 10 shows the effect of propagation distance on the protons’ energy spectrum peak position. This estimate of the peak position versus distance can be used to constrain the observed proton source distances.

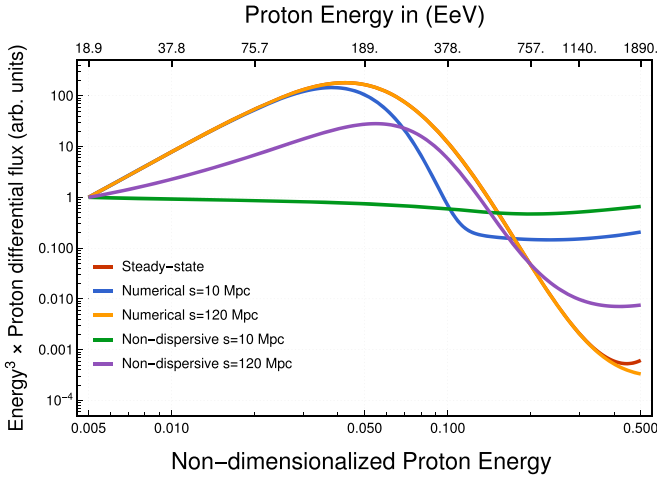


Figure 9. The steady-state potential solution (red), dispersion protons' spectrum (blue, orange), and the nondispersive spectrum (green, purple) for 10 and 120 Mpc source distances.

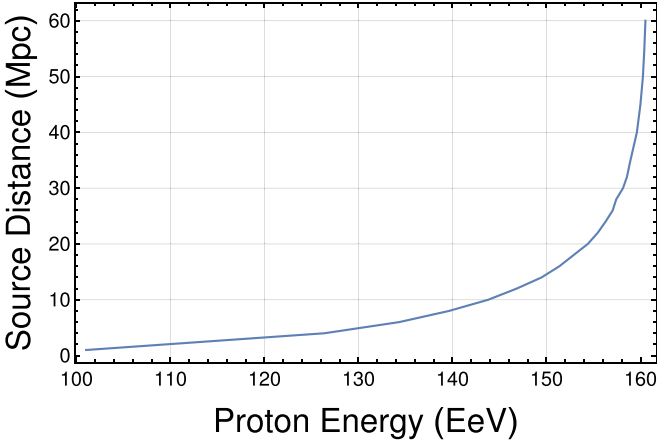


Figure 10. The propagation distance as a function of the protons' energy spectrum peak positions.

4. Conclusion

Using the Fokker–Planck potential approach, we studied the effect of energy-loss dispersion on the propagation of UHECR proton's energy spectrum. We use laboratory measurements to evaluate the systematic and dispersive energy losses (Fokker–Planck coefficients) due to the proton's interaction with the CMB photons. Additionally, we used these coefficients to transform the kinetic transport problem into a diffusion-over-a-barrier problem. The barrier is represented by a potential. In this formalism, the potential includes both systematic and dispersive energy losses in a compact insightful form.

Our results suggest that the diffusive energy losses have a significant effect on the proton's propagation; its horizon distance and the energy spectrum. Estimation of the protons' mean horizon distance using the Fokker–Planck potential shows that this distance may only extend up to 75–88 Mpc. This estimated range according to our model is somewhat lower than what has been previously thought and is a result of dispersion in energy loss.

Additionally, our model suggests that the GZK cutoff is broad and should be treated as a window or interval rather than a singly defined value. This is due to the dispersive feature of the energy losses, which results in randomizing the amount of

energy a proton may lose in each collision (interaction). This can be seen in Figure 7 for proton's energy between 8×10^{20} and 5×10^{21} eV where in this window, the probability sharply changes and follows a sigmoidal function. We estimate this broadness to span 1.5 orders of magnitude.

The Fokker–Planck potential is also used to help distinguish between protons and heavy ions based on the detected charged particle energy by assigning a characteristic probability to protons to clear the potential as a function of energy. The probability-energy curve suggests that the observed particles around the typically assumed narrow GZK cutoff energy (5×10^{19} eV) are mainly heavy ions, in agreement with Aab et al. (2014, 2016). Also, according to this curve, particles with energies larger than 8×10^{20} eV and less than 3×10^{21} eV might be a combination of protons and heavy ions. Finally, particles with energies exceeding 3×10^{21} eV are mainly protons.

A detailed modeling of the heavy ion propagation using the potential method can help distinguish, using current observations, between protons and heavy ions, as well as constrain their source distances. This will be addressed in Paper II of this series.

S.T.A. acknowledges discussions with Prof. James Matthews (LSU) on UHECR observations. G.M.W. is supported in part by NASA grant 80NSSC19K0075.

Appendix

In this appendix we outline the derivation of Equations (13) and (14). We start from the Fokker–Planck equation (Equation (7)) and the transformation of the independent variables $\xi = \xi(\epsilon)$ in Equation (11). Applying the chain rule on the first-order partial derivatives yields,

$$\frac{\partial}{\partial \epsilon} = \frac{d\xi}{d\epsilon} \frac{\partial}{\partial \xi} = \xi_\epsilon \frac{\partial}{\partial \xi}. \quad (\text{A1})$$

The Fokker–Planck equation can be written as,

$$\frac{\partial f(\epsilon, s)}{\partial s} = \frac{\partial}{\partial \epsilon} \left[-\mathcal{K}_1(\epsilon) f(\epsilon, s) + \frac{\partial}{\partial \epsilon} (\mathcal{K}_2(\epsilon) f(\epsilon, s)) \right], \quad (\text{A2})$$

Additionally, from Equation (11):

$$\xi_\epsilon = \sqrt{\frac{\mathcal{K}'_2}{\mathcal{K}_2(\epsilon)}}. \quad (\text{A3})$$

The proton energy density function in the transformed energy $\tilde{f}(\xi, s)$ is related to $f(\epsilon, s)$ via:

$$f(\epsilon, s) = \tilde{f}(\xi, s) \frac{d\xi}{d\epsilon} = \tilde{f}(\xi, s) \xi_\epsilon \quad (\text{A4})$$

Substituting Equations (A1) and (A4) into Equation (A2), we get:

$$\xi_\epsilon \frac{\partial \tilde{f}(\xi, s)}{\partial s} = \xi_\epsilon \frac{\partial}{\partial \xi} \left[-\mathcal{K}_1(\epsilon) \tilde{f}(\xi, s) \xi_\epsilon + \frac{\partial}{\partial \epsilon} (\mathcal{K}_2(\epsilon) f(\epsilon, s)) \right], \quad (\text{A5})$$

$$\xi_\epsilon \frac{\partial \tilde{f}(\xi, s)}{\partial s} = \xi_\epsilon \frac{\partial}{\partial \xi} [-\mathcal{K}_1(\epsilon) \tilde{f}(\xi, s) \xi_\epsilon + (\mathcal{K}_{2,\epsilon}(\epsilon) f(\epsilon, s) + \mathcal{K}_2(\epsilon) f_\epsilon(\epsilon, s))], \quad (\text{A6})$$

$$\frac{\partial \tilde{f}(\xi, s)}{\partial s} = \frac{\partial}{\partial \xi} \left[-\mathcal{K}_1 \tilde{f}(\xi, s) \xi_\epsilon + \mathcal{K}_2 (\xi_\epsilon)^2 \tilde{f}(\xi, s) \xi_\epsilon + \mathcal{K}_2 \tilde{f}(\xi, s) \left(\xi_{\epsilon\epsilon} + \frac{\mathcal{K}_{2,\epsilon} \xi_\epsilon}{\mathcal{K}_2} \right) \right]. \quad (\text{A7})$$

Because $\mathcal{K}'_2 = \xi_\epsilon^2 \mathcal{K}_2(\epsilon) = \text{constant}$, Equation (A7) gives:

$$\frac{\partial \tilde{f}(\xi, s)}{\partial s} = -\frac{\partial}{\partial \xi} \left[\mathcal{K}_1 \tilde{f}(\xi, s) \xi_\epsilon - \mathcal{K}_2 \tilde{f}(\xi, s) \times \left(\xi_{\epsilon\epsilon} + \frac{\mathcal{K}_{2,\epsilon} \xi_\epsilon}{\mathcal{K}_2} \right) \right] + \frac{\partial^2}{\partial \xi^2} [\mathcal{K}_2 (\xi_\epsilon)^2 \tilde{f}(\xi, s)], \quad (\text{A8})$$

where ξ_ϵ is given by Equation (A3). Now we define the transformed drift $\mathcal{K}'_1[\xi(\epsilon)]$ and diffusion \mathcal{K}'_2 coefficients,

$$\begin{aligned} \mathcal{K}'_1[\xi(\epsilon)] &= \mathcal{K}_1 - \mathcal{K}_2 \left(\xi_{\epsilon\epsilon} + \frac{\mathcal{K}'_{2,\epsilon} \xi_\epsilon}{\mathcal{K}'_2} \right) \\ &= \left(\frac{\mathcal{K}'_2}{\mathcal{K}_2(\epsilon)} \right)^{1/2} \left(\mathcal{K}_1(\epsilon) - \frac{1}{2} \frac{d\mathcal{K}_2(\epsilon)}{d\epsilon} \right), \end{aligned} \quad (\text{A9})$$

and

$$\mathcal{K}'_2 = \xi_\epsilon^2 \mathcal{K}_2(\epsilon) = \text{constant}. \quad (\text{A10})$$

Equation (A8) becomes

$$\frac{\partial \tilde{f}(\xi, s)}{\partial s} = -\frac{\partial}{\partial \xi} [\mathcal{K}'_1 \tilde{f}(\xi, s)] + \mathcal{K}'_2 \frac{\partial^2}{\partial \xi^2} [\tilde{f}(\xi, s)]. \quad (\text{A11})$$

ORCID iDs

G. M. Webb  <https://orcid.org/0000-0002-0617-9502>

References

- Aab, A., Abreu, P., Aglietta, M., et al. 2014, *PhRvD*, **90**, 122005
Aab, A., Abreu, P., Aglietta, M., et al. 2016, *PhLB*, **762**, 288295
Aab, A., Abreu, P., Aglietta, M., et al. 2018, *ApJL*, **853**, L29
Abbasi, R. U., Abe, M., Abu-Zayyad, T., et al. 2014, *ApJL*, **790**, L21
Abbasi, R. U., Abu-Zayyad, T., Allen, M., et al. 2009, *PhRvL*, **100**, 101101
Abraham, J., Abreu, P., Aglietta, M., et al. 2008, *PhRvL*, **100**, 061101
Aloisio, R., Berezhinsky, V., & Gazizov, A. 2009, *ApJ*, **693**, 1275
Anchordoqui, L. A., Romero, G. E., & Combi, J. A. 1999, *PhRvD*, **60**, 103001
Apel, W. D., Arteaga-Velázquez, J. C., Bekk, K., et al. 2011, *PhRvL*, **107**, 171104

- Armstrong, T. A., Hogg, W. R., Lewis, G. M., et al. 1972, *PhRvD*, **5**, 1640
Batista, R. A., Dundovic, A., Erdmann, M., et al. 2016, *JCAP*, **2016**, 1
Berezinsky, V. 2013, *EPJ Web of Conferences*, **53**, 01003
Berezinsky, V., & Gazizov, A. Z. 2006, *ApJ*, **643**, 8
Berezinsky, V., & Gazizov, A. Z. 2007, *ApJ*, **669**, 684
Berezko, E. G. 2008, *ApJL*, **684**, L69
Biermann, P. L., & Sigl, G. 2001, in *Physics and Astrophysics of Ultra-High-Energy Cosmic Rays*, ed. M. Lemoine & G. Sigl (Berlin: Springer)
Biermann, P. L., Caramete, L. I., Frascchetti, F., et al. 2016, *The Nature and Origin of Ultra-high Energy Cosmic Ray Particles*, Invited Review at the Vulcano Meeting, arXiv:1610.00944
Biermann, P. L., Kronberg, P. P., Allen, M. L., et al. 2019, *Galax*, **7**, 48
Blaksley, C., Parizot, E., Decerprit, G., & Allard, D. 2013, *A&A*, **552**, A125
Blümer, J., Engel, R., & Hörandel, J. R. 2009, *PrPNP*, **63**, 293
Boratav, M., & Letessier-Selvon, A. 2001, in *Physics and Astrophysics of Ultra-High-Energy Cosmic Rays*, ed. M. Lemoine & G. Sigl (Berlin: Springer)
Drury, L. O'C 2012, *Aph*, **40**, 52
Englefield, M. J. 1988, *JSP*, **52**, 369
Fedorov, Y. I., Gnatyk, R. B., Gnatyk, B. I., et al. 2016, *KPCB*, **32**, 105
Gardiner, G. W. 1983, *Handbook of Stochastic Methods for Physics, Chemistry and the Natural Science* (Berlin: Springer)
Genzel, H., Joos, P., & Pfeil, W. 1973, in *Landolt, Börnstein: Photoproduction of Elementary Particles*, ed. H. Schopper (Berlin: Springer), 8
Greisen, K. 1966, *PhRvL*, **16**, 748
Grigor'eva, S. I. 2007, *Bull. Russ. Acad. Sci.*, **71**, 454
Hanggi, P., Talkner, P., & Borkovec, M. 1990, *RvMP*, **62**, 251
Harari, D. 2014, *CRPhy*, **15**, 376
Haungs, A., Rebel, H., & Roth, M. 2003, *RPPH*, **66**, 1145
Hayakawa, S., & Yamamoto, Y. 1963, *PTHPh*, **30**, 71
Hill, C. T., & Schramm, D. N. 1985, *PhRvD*, **31**, 564
Hillas, A. M. 1984, *ARA&A*, **22**, 425
Hörandel, J. R. 2010, *PrPNP*, **64**, 351
Kampert, K.-H. 2013, *BrJPh*, **43**, 376
Kotera, K., & Olinto, A. 2011, *ARA&A*, **49**, 119
Kramers, H. A. 1940, *Phy*, **7**, 284
Letessier-Selvon, A., & Stanev, T. 2011, *RvMP*, **83**, 907
Matthews, J. H., Bell, A. R., Araudo, A. T., & Blundell, K. M. 2019, *EPJWC*, **210**, 04002
Mücke, A., Engel, R., Rachen, J. P., Protheroe, R. J., & Stanev, T. 2000, *CoPhC*, **124**, 290
Mücke, A., Rachen, J. P., Stanev, T., Protheroe, R. J., & Engel, R. 1999, *PASA*, **16**, 160
Payne, M. G. 1969, *PhRv*, **185**, 611
Protheroe, R. J., & Johnson, P. A. 1996, *Aph*, **4**, 253
Puget, J. L., Stecker, F. W., & Bredekamp, J. H. 1976, *ApJ*, **205**, 638
Rachen, J. P., & Biermann, P. L. 1993, *A&A*, **272**, 377
Rachen, J. P., Stanev, T., & Biermann, P. L. 1993, *A&A*, **272**, 161
Risken, H. 1989, *The Fokker–Planck Equation: Methods of Solution and Applications* (Berlin: Springer)
Schüssler, W. E. 1992, *The Numerical Method of Lines: Integration of Partial Differential Equations* (San Diego: Academic)
Sigl, G. 2001, in *Physics and Astrophysics of Ultra-High-Energy Cosmic Rays*, ed. M. Lemoine & G. Sigl (Berlin: Springer)
Stecker, F. W. 1968, *PhRvL*, **21**, 1016
Stecker, F. W., & Salamon, M. H. 1999, *ApJ*, **512**, 521
Tsendin, L. D. 2006, *ITPS*, **34**, 728
Wittkowski, D., & Kampert, K. H. 2018, *ApJL*, **854**, L3
Yoshida, S., & Teshima, M. 1993, *PTHPh*, **89**, 833
Zatsepin, G. T., & Kuz'min, V. A. 1966, *JETPL*, **4**, 7